JOTCS A
Journal of the Turkish Chemical Society
Section: A
Chemistry
TURKISH CHEMICAL SOCIETY

Adsorption of Nitrogen on Mn(II) Metal-Organic Framework Nanoparticles

Idongesit Justina Mbonu [1]* and Olusegun Kehinde Abiola

[1]Department of Chemistry, Federal University of Petroleum Resources, Effurun, Nigeria

Abstract: Adsorption of N_2 on mixed-ligand benzoic acid and 1, 10-phenanthroline ligand of Mn(II) metal-organic framework (MOF)–nanoparticles were demonstrated. The synthesized nanostructures are characterized by techniques such as scanning electron microscopy (SEM), fourier-transform infrared spectroscopy (FT-IR), and UV-visible spectrophotometry (UV-Vis). The pore size distribution and adsorption capacity of the synthesized MOF were investigated experimentally by measuring the N_2 adsorption isotherm at 77.3 K, and the resulting data were fitted to Brunauer-Emmett-Teller (BET), de Boer, Dubinin-Radushkevich (DR), Banet-Joyner-Halenda (BJH), Horvath-Kawazoe (HK), and also applied to Density Functional Theory (DFT) models. Excitation of the Mn-MOF nanostructure resulted in an emission at 400 nm. The DSC study reveals that this molecule has a good chemical stability. The FT-IR measurement shows a variety of functional groups that are highly coordinated. Moreover, the adsorption properties evaluated by several adsorption models compared with current adsorbent materials show Mn-MOF has superior thermal stability, a high surface area, and pore openings. Because of these findings, Mn-MOF appears to be a viable material for storing gases and energy, whether at low or high pressures.

Keywords: Metal-organic framework, nanoparticles, Mn complex, adsorption studies.

Submitted: March 23, 2021. **Accepted:** August 09, 2021.

Cite this: Mbonu IJ, Abiola OK. Adsorption of Nitrogen on Mn(II) Metal-Organic Framework Nanoparticles. JOTCSA. 2021;8(3):941-52.

DOI: https://doi.org/10.18596/jotcsa.901593.

***Corresponding author. E-mail:** mbonu.idongesit@fupre.edu.ng.

INTRODUCTION

Self- assembly (1) methodology of synthesis can be a robust (1) tool (2) for the preparation (3) of complex supramolecular (3-4) architectures with fascinating properties. Self-assembly permits greater control (1) in creating two and three-dimensional structures on account of predicting the way metal-ligand coordination sphere (5) and ligand liability direct the reactions (6) to the desired products (7). Nature utilizes different kinds of weak (8), non-covalent (9) interactions (5) like hydrogen (10) bonding, charge-charge (11), donor-acceptor (12), π-π (13), van der Waals (14), and hydrophilic and hydrophobic interactions (15), to create self-assembled complex structures with controlled shapes (16), and sizes (17). Self-assembly (3) offers a wealth of understanding processes (4) like natural life fibers (18-19), micelles (20), vesicles (21), ribbons (22), and tubes (23).

Nanoparticles are materials in the size range of 1-100 nm and can be synthesized in a variety of morphologies such as spheres, platelets, disks, rods and tubes. They have large surface area per unit volume and many functions in this small volume.

Research into complex functional organic molecules through dynamic (2) covalent bonding have brought out exploitable chemical and physical properties (24) of these molecules for exciting applications (25) within the fields of energy (4) storage, gas (23) adsorption, gas separation (24), host-guest chemistry (25) and nano-composite preparations (26). The metal ions in coordination polymers (20) are the sources of energy storage, magnetism, luminescence (13), and adsorption within the compound (27). Tailoring functionality to meet required luminescence (28), electronic, mechanical (29), and optical properties need careful control over numerous components for the

formation of self-assembled coordination (21) polymers.

This account focuses on investigating the adsorption (30) capacity of the manganese(II) supramolecular reaction induced by the benzoate ion and 1,10-phenanthroline ligands rearrangement. The two hemilabile ligands possessing different binding sites reacted with manganese metal ions resulting in a heteroligated complex compound with enhanced adsorption capacity for various applications in luminescence and energy storage (4).

In this present work, we established how porous Mn-MOF adsorb nitrogen and can be used for storing energy through comparing theoretical breakthrough curves with the experimentally observed results (11,16). The prepared Mn-MOF builds out as a crystal in all directions, exhibiting a very rigid, uniform, and precise arrangement of atoms with six-coordinate manganese(II) centers as the primary metal node. The carboxylate ligands adopt monodentate and bidentate coordination modes. Because of their affinity for oxygen atoms, they are often used to synthesize functional metal complexes. 1, 10-phenanthroline was in-cooperated to the backbone of the carboxylate ligand to prevent the coordination of more water molecules with the manganese(II) metal ions.

The electronic properties of this six-coordinate Mn(II) center make this MOF reactive towards nitrogen, creating a stronger M–N_2 interaction. The coordination sites saturated with Mn-MOF nanoparticles cannot interact with nitrogen gases (22) easily. The high density of Mn(II) shows a high gas uptake capacity, making Mn- MOF a promising N_2 adsorbent (31) capacity for various applications in the areas of luminescence and energy storage (4). Different adsorption isotherm models (22) were used to evaluate the adsorption (31) capacity of the Mn-MOF and its pore filling towards applications for adsorbent-based chillers, heat pumps, and gas storage (8,32).

MATERIALS AND METHODS

All the chemicals utilized in this work are of reagent grade (8) and used as obtained. The elemental composition of Mn-MOF was performed on Perkin-Elmer 2400 elemental analyzer. Morphology of the prepared compound was carried out on a Zeiss Supra (32) instrument with a resolution of 5 nm at 30 kV (8). Vibration bands within Mn-MOF were determined using a Nicolet Magna (33) FT-IR spectrometer within the range of 4000–400 cm^{-1}.

The surface area, pore size, and pore diameter of the Mn-MOF were evaluated by measuring the N_2 adsorption isotherms (13) at "77.3 K" using an iQMicropore-XR (Quantachrome Instruments, FL, USA). Prior to the experiment, the sample was outgassed (31) under vacuum at 120 °C (33).

A single crystal Mn-MOF (0.05 mm x 0.54 mm x 0.60 mm) was selected and mounted on a cryoloop for structure determination on a Bruker DUO APEX II CCD diffractometer using graphite-monochromatic Mokα (λ =0 .71073 Å) Oxford Cryostream-700. The structure was solved by a direct method in SHELXT-2018/3 (34).

Self-assembly of Mn-MOF nanoparticles

Mn-MOF was prepared as shown in Figure 1. The mixture of $MnCl_2.4H_2O$ (0.5 mmol) and benzoic acid (0.1 mmol) in 20 mL aqueous solution was stirred for 5 minutes at 50 °C. NaOH (1 mol/L) solution was used to maintain the hydrogen ion concentration of the reaction mixture. A 5-mL alcoholic solution of 1, 10-phenanthroline (1.5 mmol) was added with stirring for 3 hours at 50 °C. On the fifth day, pale yellow crystals were observed to have separated from the mother liquor in the reaction vessel (31,35). The elemental analysis result shows that the C, H, Mn, and O are 50.50, 4.20, 16.50, and 28.80 (calc.) and 50.48, 4.27, 16.40, and 28.85 (found), respectively.

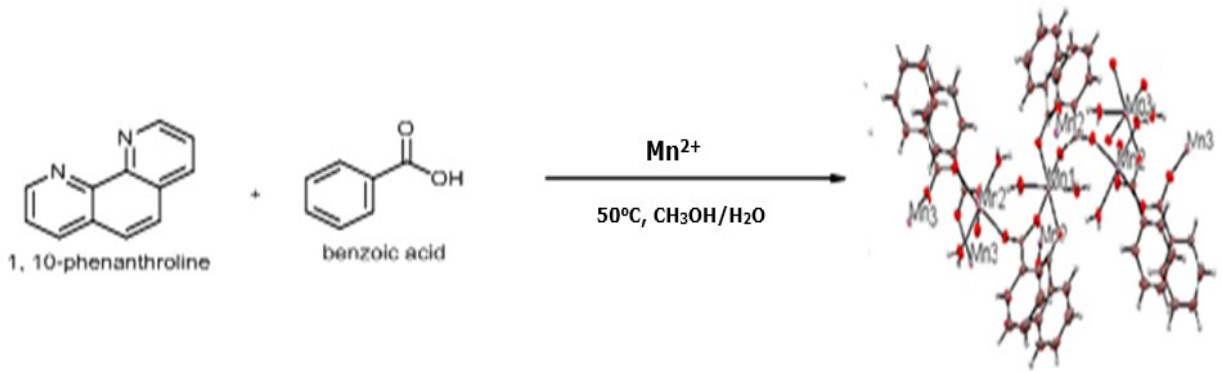

Figure 1: Graphical reaction pathway to Mn-MOF nanoparticles.

RESULTS

The one-pot synthesis of yellow Mn-MOF single crystal analysis in Figure 2a shows a 3D microporous supramolecular network constructed by 2D-layered Mn-MOF with related crystallographic data (8) listed in Table 1. The diffractogram in Figure 2b & 2c shows that the Mn-MOF crystallized in a triclinic space group P-1(31). The asymmetric unit displayed a monodentate benzoate ligand, two 1, 10-phenanthroline ligands, and a coordinated water molecule**.** The Mn(II) ion is six coordinated (32) by four nitrogen atoms from two (32) 1,10-phenanthroline ligands, one oxygen atom (15) from the carboxylate group of benzoate ligand, and one oxygen atom (31) from coordinated water molecule resulting in a distorted octahedral shape. Neighboring benzoate and phenyl groups are interlinked through π-π stacking interactions (25).

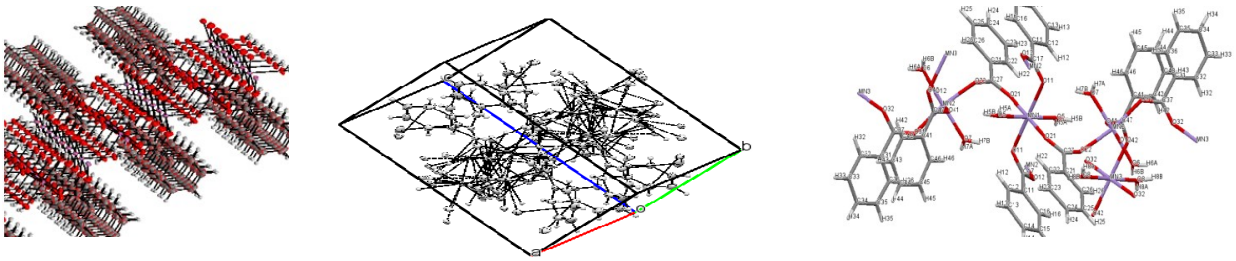

(a) (b) (c)

Figure 2: a) Projection along 'a' axis of the three-dimensional framework showing the cavities b) Molecular packing along the b axis c) ORTEP drawing of Mn-MOF.

Table 1: Crystal data, data collections, and refinement of Mn(II)-MOF at 200 K.

Crystal Data	
Empirical formula	$C_{28}H_{28}Mn_2O_{12}$
Formula weight	666.38
Unit Cell Weight	1332.77 [Based on SHELXL2014 Atomic Weights]
Crystal system	Triclinic
Space group	P-1(No.2)
a/Å, *α*/°	7.4369(3), 88.847(2)
b/Å, *β*/°	12.9898(6), 82.518(2)
c/Å, *γ*/°	14.1176(6), 89.975(2)
Volume/Å^3	1351.93(10)
Z	*2*
ρ_{calc}/g cm^{-3}	1.637
μ/mm^{-1}	1.001
F(000)	684 [calc. 685.70]
Crystal size/mm^3	0.05 x 0.54 x 0.60
Wavelength/Å	

Data Collection	
Temperature/K	200
Theta Min-Max/°	1.6, 28.4
Dataset /restraints/parameters	-9: 9; -16: 17; -18: 18
Tot., Uniq. Data, R(int)	49223, 6713, 0.025
Observed Data [$I \geq 2.0\sigma(I)$]	5021
Refinement	
Nref, Npar	6713, 414
R, wR2, S	
w = ^2^(FO^2^) +(0.0551P)^2^+1.0319 P] Where P=(FO^2^+2FC^2^)/3'	0.0353, 0.1092, 1.05
Max. and Av. Shift/Error	0.00, 0.00
Min. and Max. Resd. Dens. [e/Ang^3]	-0.56, 1.34
Radiation/ Å MoKα	0.71073

Micro-sized structures seen in the SEM image in Figure 3 are plate-like sizes and have porous surface area, implying that Mn-MOF will have high nitrogen adsorption capacity (35). Figure 4 shows the fluorescent spectrum, measured within the range of 300-800 nm, shifting to a longer wavelength with an emission maximum of 400 nm (23).

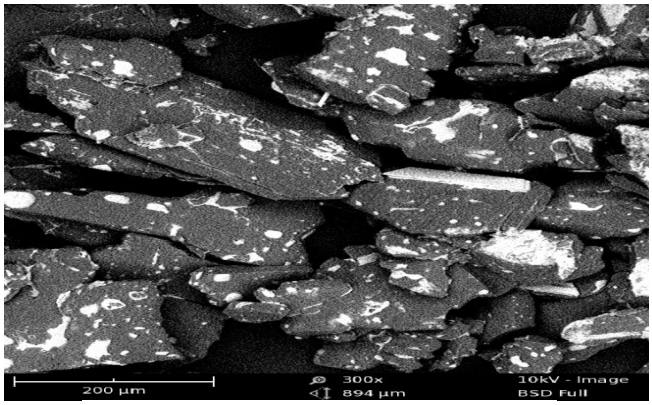

Figure 3: SEM micrograph of Mn-MOF.

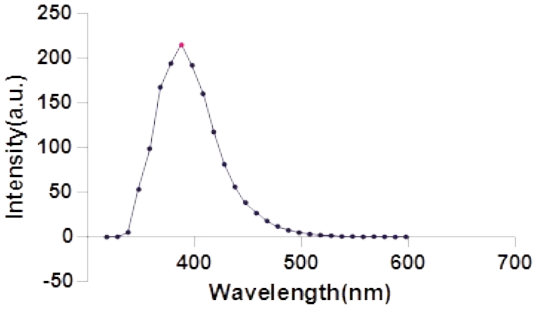

Figure 4: Spectrum at λ_{ex} = 308 nm.

The infrared spectrum of Mn-MOF in Figure 5 shows vibration bands within the range (13) of 3100-3753 cm^{-1} for *v*(OH) (13) and 842–920 cm^{-1} for σ(OH) (Kupgan *et al*., 2019), an indication of coordinated water (13) in Mn-MOF. The complex exhibits N-H stretching within the range of 2753-3373 cm^{-1}. The asymmetric and symmetric stretching frequencies of carboxylate (29) ions are shown within the range of 1688-1618 $cm^{-1}$and 1416-1282 cm^{-1} (22). The characteristic IR bands of the Mn(II) complex appear at 1688 cm^{-1} (C=O) (30) and 3373 cm^{-1} (H_2O) (23). The N-N stretching frequency (29) of the complex appeared at 779-708 cm^{-1} (29) is associated with the bidentate bridging nature of neutral ligands. These results are an indication that Mn-MOF was successfully synthesized.

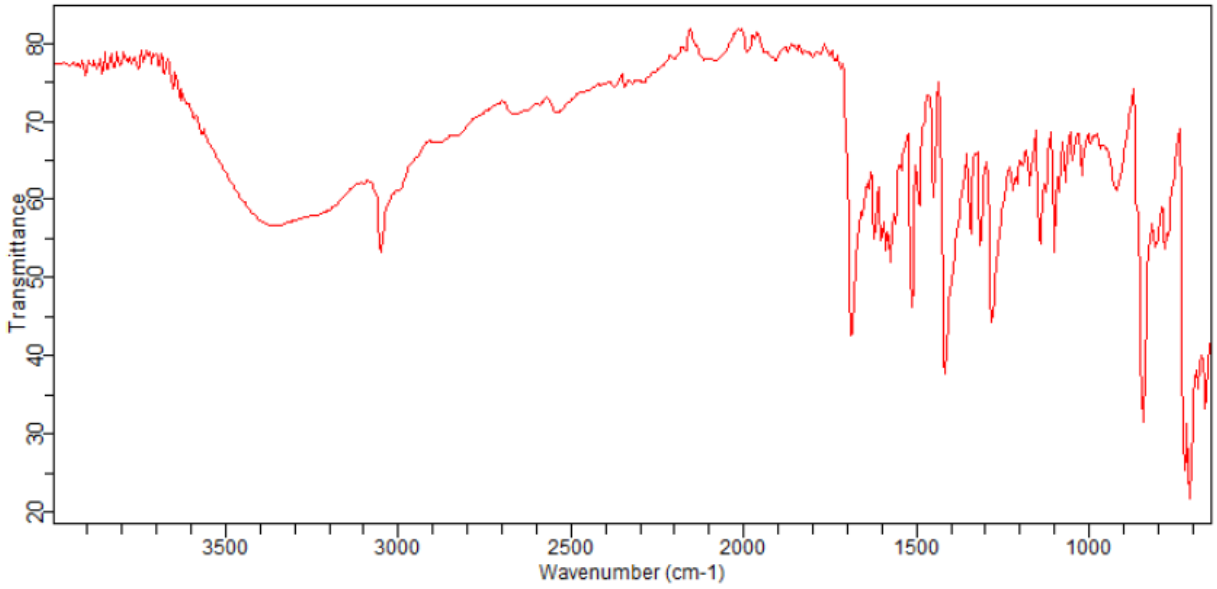

Figure 5: FT-IR spectrum of Mn-MOF.

Figure 6 shows the Brunauer-Emmett-Teller (BET) single- multilayer adsorption/desorption isothermal plot of Mn-MOF at 77.3 K (Table 2). The correlation coefficient (R^2= 0.992) and surface area using the BET model was determined by the following linear expression in Equation 1 (22):

$$\frac{1}{W\left[\left(\frac{P_o}{P}\right)-1\right]} = \frac{1}{WmC} + \frac{C-1}{W_mC}\left(\frac{P_o}{P}\right) \quad \text{(Eq. 1)}$$

Where W = weight of gas adsorbed, P/P_0 = relative pressure, W_m = weight of adsorbate as a monolayer, C = BET constant. Slope (s), intercept (i), and weight (Wm) were determined from Equation 2 below:

$$s=\frac{C-1}{W_mC}\ i=\frac{1}{W_mC}\ W_m=\frac{1}{s+i} \quad \text{(Eq. 2)}$$

Total surface area (St) was calculated from expression (Equation 3):

$$S_t=\frac{W_mN\,A_{cs}}{M} \quad \text{(Eq. 3)}$$

N = Avogadro's number ($6.023x10^{23}$), M = Molecular weight of Adsorbate (28.013), A_{cs} = Adsorbate cross-sectional area (16.2 $Å^2$ for Nitrogen). Specific Surface Area (S) (23) is then determined by the total surface area (23) by sample weight in Equation 4:

$$S=\frac{S_t}{W} \quad \text{(Eq. 4)}$$

The experimentally determined surface area with the BET model = 825.465 m^2g^{-1} which is large compared to some natural porous (18) materials, such as clay (10-100 m^2g^{-1}) (19), activated graphite (119 m^2g^{-1}), and other types of zeolite and porous carbons (18, 23).

Langmuir's experimental data plot (Figure 7) features a broader plateau region of the loop, which extends up to relatively high P/P_0. The optimization of relative pressure within the range of 0.00E+00 -3.50E-02 in Figure 7 shows that adsorption increased with increasing relative pressure, and at 1.71, the adsorption process was maximum with 84.62 % and then slightly decreases and practically constant till relative pressure 3.00E-01. The lesser adsorption at lower relative pressure could be attributed to lesser surface sites available for sorption (22). This model was used to investigate the sorption capacity of Mn-MOF using the linear expression in Equation 3:

$$\frac{1}{V_a[\frac{P_o}{P}-1]}=\frac{C-1}{V_m C}\times\frac{P}{P_0}+\frac{1}{V_m C} \quad \text{(Eq. 5)}$$

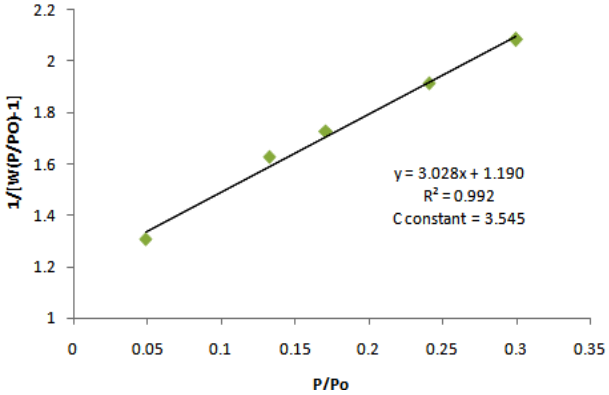

Figure 6: BET Single-multilayer nitrogen adsorption isotherm of Mn-MOF.

Where P= partial vapor pressure (33) of adsorbate, P_o = saturated pressure of adsorbate.

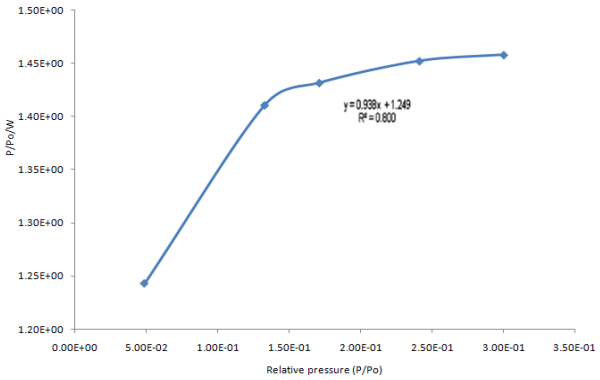

Figure 7: Langmuir plot of N_2 on Mn-MOF at 77.3K.

Figure 8 shows the isotherm plot of volume at STP (cc/g) against relative pressure shows a linear fitting result with a strong correlation of +1, indicating a perfect positive linear relationship. The estimated micropore volume of Mn-MOF from this model is found to be 5.151cc/g (14).

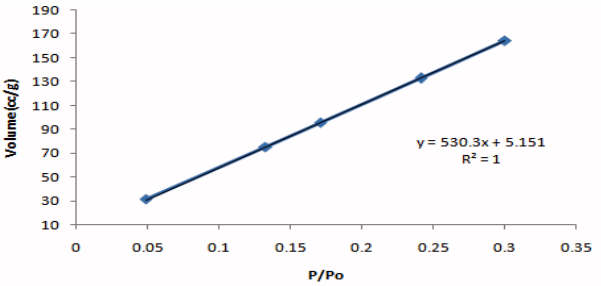

Figure 8: A linear form of Langmuir isotherm.

Figure 9 shows a linear correlation between the volumes adsorbed with statistical thickness. The t values were determined using the Halsey equation in Eq.6 &7 (26):

$$t(\text{Å})=\left[\frac{13.99}{0.034-log\frac{P}{P_0}}\right]^{0.5} \quad \text{(Eq. 6)}$$

$$t=\frac{V_{liq}}{S}\quad x\quad 10^4(\text{Å}) \quad \text{(Eq. 7)}$$

Where S is the total surface area (26) and V_{liq} is the adsorbed liquid volume (27); V_{liq} = V_{ads} (STP) x 15.47 for nitrogen adsorption at 77.3 K(26). The T- method for external surface area analysis calculated from the slope (Equation 1) gives surface area comparable to BET values (29), showing an agreement between the two methods.

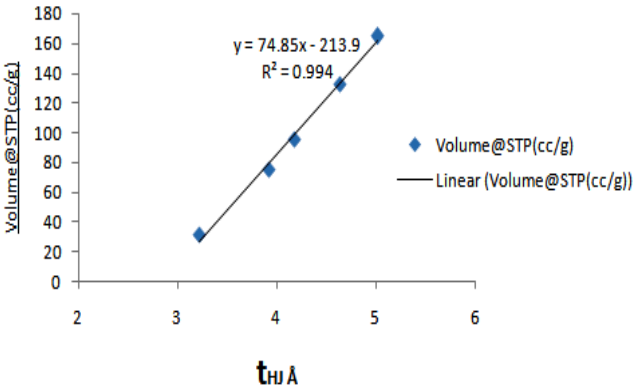

Figure 9: Temkin Adsorption isotherm for Mn-MOF.

Dubinin-Radushkevch (DR)-plot by expression (4) gave information on the micropore volume (13). The shape of the experimental Logarithm weight adsorbed plot against Log^2P/P_o (Figure 10) results in a linear uniform Gaussian distribution with a negative intercept and negative slope. The adsorption energy, average pore width, micropore volume, and micropore surface area of the Mn-MOF were determined from Equation 8, Table 2 (24):

$$W=W_0\exp\left[-\left(\frac{A}{\beta E_o}\right)\right]^2 \quad \text{(Eq. 8)}$$

$$A=-\Delta G=RT\ln\left(\frac{P_0}{P}\right), E=\beta E_0 \quad \text{(Eq. 8a)}$$

Where, β =affinity coefficient (0.3300), A = adsorption potential, DR exp(n)= 2.000, E = characteristic adsorption energy, W and W_o are amount adsorbed at P/Po and the micropore volume, respectively.

The PSD (Table 3) from the experimental adsorption (20) isotherm $N_{exp}\left(\frac{P}{P_o}\right)$ were determined from Equation 9 (20). The experimental isotherm (Table 3) is represented in

Figures 11a & b as differential (left) and cumulative (right) distributions. Figure 11b shows pore size distribution (21) calculated by QSDFT and NLDFT (22) methods to overlap generously, indicating that both methods give similar results despite different approaches. Both methods show the three-peak distribution of micropores region with sizes 1.93 and 2.31-2.64 nm. The smallest pore size on QSDFT PSD, as expressed in Equation 9, is 1.68 nm resulting in not fully resolved peak in low pore size range with an L-curve (27).

$$N_{exp}\left(\frac{P}{P_o}\right)=\int_{Dmin.}^{Dmax.} N_{QSDFT}\left(\frac{P}{P_o},\ D\right)F(D)\,dD \quad \text{(Eq. 9)}$$

Where: $N\left(\frac{P}{P_o},W\right)$ = experimental adsorption isotherm data, W = pore width, $N_{exp}\left(\frac{P}{P_o}\right)$ = isotherm on a single pore of width W, f(W) = pore size distribution function. Here D_{min} and D_{max} are the minimum and maximum pore sizes (31) in the kernel, respectively.

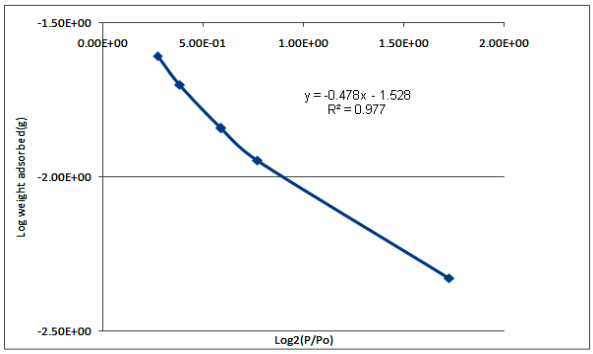

Figure 10: Dubinin-Radushkevich adsorption isotherm for Mn-MOF.

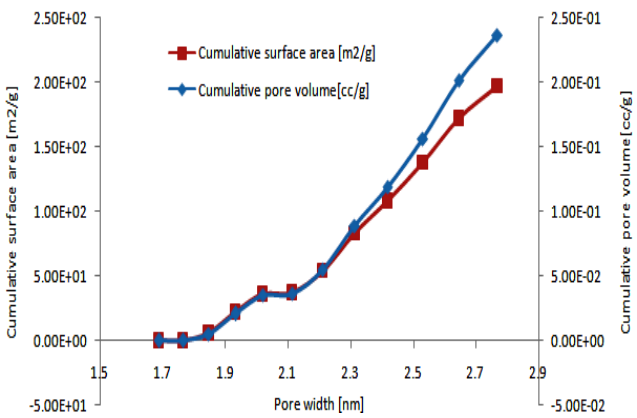

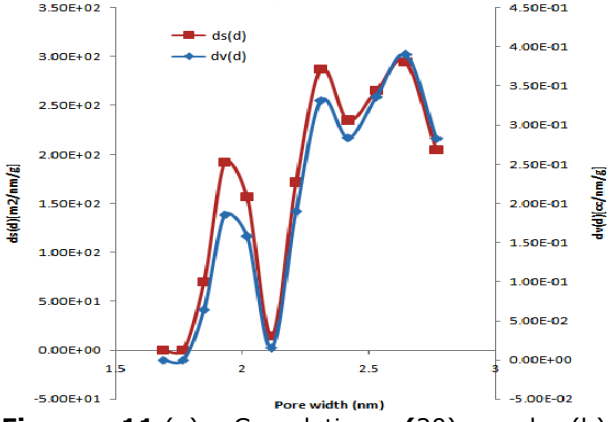

Figure 11.(a) Cumulative **(**20) and (b) differential cumulative pore volume (19) and cumulative surface area distributions of Mn -MOF on carbon slit pore from N_2 adsorption isotherms at 77.3 K (19) using NLDFT equilibrium mode.

Table 2: Nitrogen adsorption on Mn-MOF.

P/Po	Volume at STP (cc/g)	1/[W(Po/P)-1)]	P/Po/W	$Log_2(P/Po)$	Weight adsorbed [(g)]	Statistical thickness, Å
4.85E-02	31.2535	1.31E+00	1.24E+00	1.73E+00	4.69E-03	3.221736914
1.33E-01	75.3158	1.63E+00	1.41E+00	7.69E-01	1.13E-02	3.919188098
1.71E-01	95.5990	1.73E+00	1.43E+00	5.88E-01	1.43E-02	4.179641641
2.41E-01	132.8608	1.91E+00	1.45E+00	3.82E-01	1.99E-02	4.633363309
3.00E-01	164.7080	2.08E+00	1.46E+00	2.73E-01	2.47E-02	5.013433024

Table 3: DFT & NDFLT Pore Analysis.

Pore width [nm]	Cumulative pore volume [cc/g]	Cumulative surface area [m^2/g]	dv(d) [cc/nm/g]	ds(d) [m^2/nm/g]
1.6879	0.00E+00	0.00E+00	0.00E+00	0.00E+00
1.7656	0.00E+00	0.00E+00	0.00E+00	0.00E+00
1.8469	5.23E-03	5.66E+00	6.43E-02	6.96E+01
1.9319	2.10E-02	2.20E+01	1.85E-01	1.92E+02
2.0208	3.50E-02	3.59E+01	1.58E-01	1.56E+02
2.1138	3.64E-02	3.72E+01	1.51E-02	1.43E+01
2.2111	5.49E-02	5.39E+01	1.90E-01	1.72E+02
2.3129	8.87E-02	8.31E+01	3.32E-01	2.87E+02
2.4194	1.19E-01	1.08E+02	2.84E-01	2.35E+02
2.5307	1.56E-01	1.38E+02	3.36E-01	2.65E+02
2.6472	2.02E-01	1.72E+02	3.90E-01	2.95E+02
2.7691	2.36E-01	1.97E+02	2.83E-01	2.05E+02

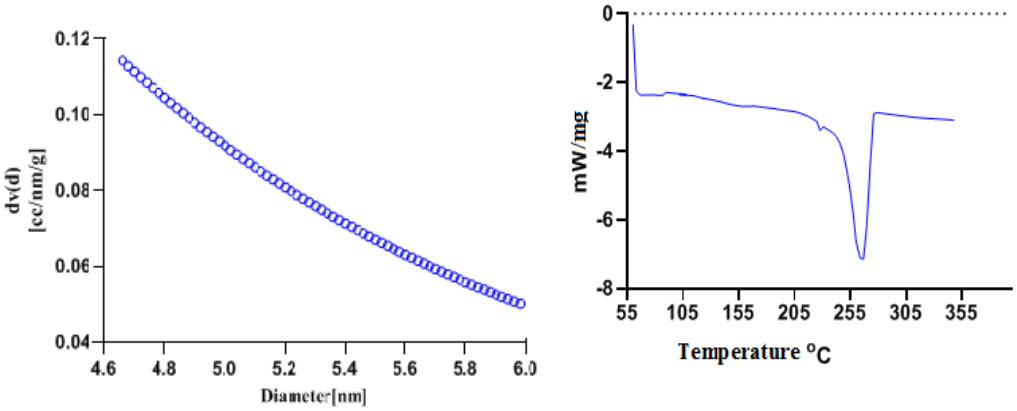

Figure 12: (a) shows the pore size distribution and (b) shows the DSC plot with a depression at 264.43 °C (– 7.20 mW) , ΔH +107.00 KJ/mol (ΔH +551.00J/g).

Table 4 gives the micropore analysis by Dubinin-Radushkevich (DR), Horvath-Kawazoe (HK), and Dubinin-Astakhov (DA) methods. Dollimore and Heal (DH) (20) were used to estimate the pore size distribution (13). The pore–size distribution (18) is obtained by applying the BJH (Barret, Joyner, and Halenda) technique.

DISCUSSION

The Langmuir surface area of 4374 m^2g^{-1} after activation shows a high permanent porosity with an octahedrally coordinated environment. FT-IR spectrum results show that Mn-MOF has well-populated functional groups that form a strong coordination network for storage purposes. The Mn-MOF exhibits a pore size of 6.077 nm and pore volume of 2.920 nm displaying a highly porous and high nitrogen uptake capacity.

CONCLUSION AND RECOMMENDATIONS

These findings are consistent with literature reviews and adsorption experiments published by a number of authors revealing the storing capacity of metal-organic frameworks'. This work describes a novel synthetic method for preparing self-assembled porous metal-organic frameworks with potential energy storage capabilities.

We use several adsorption isotherms to investigate the storage and adsorption capacity of the Mn-MOF produced in this study. We performed DSC, SEM, single-crystal diffraction studies, FTIR, fluorescence, and UV-visible spectrophotometry to characterize this compound. The strong storing and adsorption capacity of the manganese(II) nanoparticles is revealed by experimental findings and evaluation adsorption capacity of this compound under some adsorption isotherms. The Mn-MOF surface area is currently being optimized for hydrogen and carbon capture.

CONFLICT OF INTEREST

The authors declare the nonexistence of any conflicts of interest

AUTHORS' CONTRIBUTION

This work was carried out in collaboration between both authors. IJM designed the study, carried out analyses. IJM and KOA wrote the manuscript for publication

FUNDING

This work was supported by the Tertiary Education Trust Fund (RE: FUPRE/TO/RESR/2017/01), Nigeria.

ACKNOWLEDGMENTS

The authors wish to acknowledge single-crystal structure analysis by Summerstrand Campus South, northwest University South Africa..

Table 4: Adsorption properties of Mn-MOF given by different Isotherm Models.

Adsorption Models	Surface Area (m^2g^{-1})	Pore Size (nm)	Pore Volume ccg^{-1}	Slope	Adsorption energy KJ/mol	C constant	Average pore width (nm)	Pore Diameter (nm)	Intercept	Best n	R^2
SinglePoint BET	5.017 E+02			3.029					1.190 E+00		0.9960
MultiPoint BET	8.255 E+02			3.029		3.545			1.190 E+00		
Langmuir	4.374 E+03			0.79612					1.25689		0.8650
Barrett, Joyner, and Halenda Method (BJH)	9.570 E+02	2.093	4.614 E-01						2.093 E+00		
Dollimore and Heal (DH)	1.034 E+03	2.093	4.776 E-01						2.093 E+00		
T-method	8.255 E+02										0.9940
Dubinin Radushkevich method (DR)	8.601E+02	6.077	3.056 E-01	-4.780 E-01	4.279		6.077 E+00		2.964E-02	2.000	0.9770
Density Functional Theory (DFT)	196.913		0.236						2.647		
Dubinin-Astakhov Method (DA)		2.920			0.707			2,92E+00	2.964E-02	1.000	
Horvath-Kawazoe (HK)		1.882	1.326 E-01						1.882 E+00		
SF		3.534	2.708 E-02						3.534 E+00		

REFERENCES

1. Chakrabarty R, Mukherjee PS, Stang PJ. Supramolecular Coordination: Self-Assembly of Finite Two- and Three-Dimensional Ensembles. Chem Rev. 2011 Nov 9;111(11):6810–918. <DOI>.

2. Agthe M, Høydalsvik K, Mayence A, Karvinen P, Liebi M, Bergström L, et al. Controlling Orientational and Translational Order of Iron Oxide Nanocubes by Assembly in Nanofluidic Containers. Langmuir. 2015 Nov 17;31(45):12537–43. <DOI>.

3. Sun Y, Zhang F, Jiang S, Wang Z, Ni R, Wang H, et al. Assembly of Metallacages into Soft Suprastructures with Dimensions of up to Micrometers and the Formation of Composite Materials. J Am Chem Soc. 2018 Dec 12;140(49):17297–307. <DOI>.

4. Shoji S, Ogawa T, Matsubara S, Tamiaki H. Bioinspired supramolecular nanosheets of zinc chlorophyll assemblies. Sci Rep. 2019 Dec;9(1):14006. <DOI>.

5. Jin Y, Wang Q, Taynton P, Zhang W. Dynamic Covalent Chemistry Approaches Toward Macrocycles, Molecular Cages, and Polymers. Acc Chem Res. 2014 May 20;47(5):1575–86. <DOI>.

6. Ion AE, Nica S, Madalan AM, Shova S, Vallejo J, Julve M, et al. Two-Dimensional Coordination Polymers Constructed Using, Simultaneously, Linear and Angular Spacers and Cobalt(II) Nodes. New Examples of Networks of Single-Ion Magnets. Inorg Chem. 2015 Jan 5;54(1):16–8. <DOI>.

7. Springer MA, Liu T-J, Kuc A, Heine T. Topological two-dimensional polymers. Chem Soc Rev. 2020;49(7):2007–19. <DOI>.

8. Bandosz TJ, Petit C. MOF/graphite oxide hybrid materials: exploring the new concept of adsorbents and catalysts. Adsorption. 2011 Feb;17(1):5–16. <DOI>.

9. Zhang S. Fabrication of novel biomaterials through molecular self-assembly. Nat Biotechnol. 2003 Oct;21(10):1171–8. <DOI>.

10. Guo J, Tardy BL, Christofferson AJ, Dai Y, Richardson JJ, Zhu W, et al. Modular assembly of superstructures from polyphenol-functionalized building blocks. Nature Nanotech. 2016 Dec;11(12):1105–11. <DOI>.

11. Piot M, Abécassis B, Brouri D, Troufflard C, Proust A, Izzet G. Control of the hierarchical self-assembly of polyoxometalate-based metallomacrocycles by redox trigger and solvent composition. Proc Natl Acad Sci USA. 2018 Sep 4;115(36):8895–900. <DOI>.

12. Bose A, Mal P. Mechanochemistry of supramolecules. Beilstein J Org Chem. 2019 Apr 12;15:881–900. <DOI>.

13. Kupgan G, Abbott LJ, Hart KE, Colina CM. Modeling Amorphous Microporous Polymers for CO 2 Capture and Separations. Chem Rev. 2018 Jun 13;118(11):5488–538. <DOI>.

14. Jiang H-L, Liu B, Lan Y-Q, Kuratani K, Akita T, Shioyama H, et al. From Metal–Organic Framework to Nanoporous Carbon: Toward a Very High Surface Area and Hydrogen Uptake. J Am Chem Soc. 2011 Aug 10;133(31):11854–7. <DOI>.

15. Zhao Y, Song Z, Li X, Sun Q, Cheng N, Lawes S, et al. Metal organic frameworks for energy storage and conversion. Energy Storage Materials. 2016 Jan;2:35–62. <DOI>.

16. Wu HB, Lou XW (David). Metal-organic frameworks and their derived materials for electrochemical energy storage and conversion: Promises and challenges. Sci Adv. 2017 Dec;3(12):eaap9252. <DOI>.

17. Dey C, Kundu T, Biswal BP, Mallick A, Banerjee R. Crystalline metal-organic frameworks (MOFs): synthesis, structure and function. Acta Crystallogr B Struct Sci Cryst Eng Mater. 2014 Feb 1;70(1):3–10. <DOI>.

18. Aizuddin M MA, Yin C-Y, Mikhail Sa R. Analysis of the Textural Characteristics and Pore Size Distribution of a Commercial Zeolite using Various Adsorption Models. J of Applied Sciences. 2011 Oct 15;11(21):3650–4. <DOI>.

19. Seredych M, Bandosz TJ. Manganese oxide and graphite oxide/MnO2 composites as reactive adsorbents of ammonia at ambient conditions. Microporous and Mesoporous Materials. 2012 Mar;150:55–63. <DOI>.

20. Landers J, Gor GYu, Neimark AV. Density functional theory methods for characterization of porous materials. Colloids and Surfaces A: Physicochemical and Engineering Aspects. 2013 Nov;437:3–32. <DOI>.

21. Ravikovitch PI, Vishnyakov A, Russo R, Neimark AV. Unified Approach to Pore Size

Characterization of Microporous Carbonaceous Materials from N 2 , Ar, and CO 2 Adsorption Isotherms †. Langmuir. 2000 Mar;16(5):2311–20. <DOI>.

22. Foo KY, Hameed BH. Insights into the modeling of adsorption isotherm systems. Chemical Engineering Journal. 2010 Jan 1;156(1):2–10. <DOI>.

23. Wang LH, Li PF. Synthesis, Structure, and Catalytic Activity of A New Mn(II) Complex with 1,4-Phenylenediacetic Acid and 1,10-Phenanthroline. Bull Chem React Eng Catal. 2018 Apr 2;13(1):1. <DOI>.

24. Li L-J, Lau DSP, De Gendt S, Ren F. Properties and Applications of 2-Dimensional Layered Materials. ECS J Solid State Sci Technol. 2016;5(11):Y7–Y7. <DOI>.

25. Jiang J, Yaghi OM. Brønsted Acidity in Metal–Organic Frameworks. Chem Rev. 2015 Jul 22;115(14):6966–97. <DOI>.

26. Lowell S, Shields J, Thomas M, Thommes M, editors. Characterization of porous solids and powders: surface area, pore size and density. 4. ed., 1. reprint with some corr. Dordrecht: Springer; 2006. 347 p. (Particle technology series). ISBN: 978-1-4020-2303-3 978-1-4020-2302-6.

27. Lv Y, Shi P, Shen W, Chen X, Zhao G. A series of novel Zn(II) and Mn(II) metal-organic frameworks constructed by 2,4-bis-oxyacetate-benzoic acid: syntheses, structures and photoluminescence. Sci China Chem. 2015 Mar;58(3):448–56. <DOI>.

28. Gawas UB, Verenkar VMS, Mojumdar SC. Nano-crystalline Mn0.3Ni0.3Zn0.4Fe2O4 obtained by novel fumarato-hydrazinate precursor method: Synthesis, characterization and studies of magnetic and electrical properties. J Therm Anal Calorim. 2012 Jun;108(3):865–70. <DOI>.

29. Sasmal HS, Halder A, Kunjattu H S, Dey K, Nadol A, Ajithkumar TG, et al. Covalent Self-Assembly in Two Dimensions: Connecting Covalent Organic Framework Nanospheres into Crystalline and Porous Thin Films. J Am Chem Soc. 2019 Dec 26;141(51):20371–9. <DOI>.

30. Mokhatab S, Poe WA, Mak JY. Handbook of natural gas transmission and processing: principles and practices. Fourth edition. Cambridge, MA: Gulf Professional Publishing; 2019. 826 p. ISBN: 978-0-12-815817-3.

31. Li Y-L, Zhao Y, Wang P, Kang Y-S, Liu Q, Zhang X-D, et al. Multifunctional Metal–Organic Frameworks with Fluorescent Sensing and Selective Adsorption Properties. Inorg Chem. 2016 Nov 21;55(22):11821–30. <DOI>.

32. Balzer C, Cimino RT, Gor GY, Neimark AV, Reichenauer G. Deformation of Microporous Carbons during N 2 , Ar, and CO 2 Adsorption: Insight from the Density Functional Theory. Langmuir. 2016 Aug 16;32(32):8265–74. <DOI>.

33. Mabayoje O, Seredych M, Bandosz TJ. Enhanced adsorption of hydrogen sulfide on mixed zinc/cobalt hydroxides: Effect of morphology and an increased number of surface hydroxyl groups. Journal of Colloid and Interface Science. 2013 Sep;405:218–25. <DOI>.

34. Tahier T, Oliver CL. In situ variable-temperature single crystal X-ray diffraction studies of the single-crystal-to-single-crystal dehydration and rehydration of a mixed-ligand 2D zinc metal–organic framework using trimesate and 4,4′-bipyridine- N , N ′-dioxide as ligands. CrystEngComm. 2015;17(46):8946–56. <DOI>.

35. Justina Mbonu I. Synthesis, Crystal Structure and Photoluminescence Properties of Diaquabis (1,10Phenanthroline, κ,N,N′)(Benzoato-κ,O) Manganese(II)Dihydrate. OMCIJ [Internet]. 2020 Jul 28 [cited 2021 Aug 10];9(5): 555773. <DOI>.